small methods
www.small-methods.com

Robust Preparation of Sub-20-nm-Thin Lamellae for Aberration-Corrected Electron Microscopy

*Hideyo Tsurusawa, Jun Uzuhashi, Yusuke Kozuka, Koji Kimoto, and Tadakatsu Ohkubo**

Aberration-corrected scanning transmission electron microscopy (STEM) has been advancing resolution, sensitivity, and microanalysis due to the intense demands of atomic-level microstructural investigations. Recent STEM technologies require preparing a thin lamella whose thickness is ideally below 20 nm. Although focused-ion-beam/scanning-electron-microscopy (FIB/SEM) is an established method to prepare a high-quality lamella, nanometer-level controllability of lamella thickness remains a fundamental problem. Here, the robust preparation of a sub-20-nm-thin lamella is demonstrated by FIB/SEM with real-time feedback from thickness quantification. The lamella thickness is quantified by back-scattered-electron SEM imaging in a thickness range between 0 and 100 nm without any reference to numerical simulation. Using real-time feedback from the thickness quantification, the FIB/SEM terminates thinning a lamella at a targeted thickness. The real-time feedback system eventually provides 1-nm-level controllability of the lamella thickness. As a proof-of-concept, a near-10-nm-thin lamella is prepared from a $SrTiO_3$ crystal by our methodology. Moreover, the lamella thickness is controllable at a target heterointerface. Thus, a sub-20-nm-thin lamella is prepared from a $LaAlO_3/SrTiO_3$ heterointerface. The methodology offers a robust and operator-independent platform to prepare a sub-20-nm-thin lamella from various materials. This platform will broadly impact aberration-corrected STEM studies in materials science and the semiconductor industry.

1. Introduction

Aberration-corrected scanning/transmission electron microscopy (S/TEM) is widely used for atomic-level imaging and microanalysis in materials science and the semiconductor industry.[1–4] STEM has been intensively advancing in its resolution,[2,5] sensitivity to light elements,[6–8] and microanalysis of chemical status by electron energy loss spectroscopy (EELS).[9–16] Meanwhile, these state-of-the-art STEM technologies require a high-quality lamella with minimum damage and a thickness ideally below 20 nm.[2,5,11] However, it is difficult to prepare such a thin lamella from a bulk material with nanometer-level controllability of its thickness. Eventually, the lamella preparation limits the practical applications of aberration-corrected STEM.

Focused-ion-beam/scanning-electron-microscope (FIB/SEM) is a common method for preparing a high-quality lamella from bulk material.[17–22] In a standard protocol, FIB cuts a micron-sized chunk in a bulk material, transfers the chunk to a TEM grid by an in situ manipulator, and finally thins the chunk. Since a high-quality lamella needs to minimize surface damage, the FIB acceleration voltage is lowered to 2 kV or below in the final thinning process.[19,20] Hence, FIB can prepare a lamella with minimum damage.

The controllability of a lamella thickness has been a fundamental problem in the FIB/SEM method to prepare a thin lamella. FIB/SEM can monitor the lamella condition by SEM imaging when the FIB is thinning the lamella (**Figure 1a**). An operator usually sees a secondary-electron SEM image of the lamella and manually interprets its electron transparency to the lamella thickness. Although SEM imaging helps determine the endpoint of the FIB thinning process, this

H. Tsurusawa
LQUOM Inc.
79-5, Tokiwadai, Hodogaya, Yokohama 240-8501, Japan

The ORCID identification number(s) for the author(s) of this article can be found under https://doi.org/10.1002/smtd.202301425

DOI: 10.1002/smtd.202301425

J. Uzuhashi, T. Ohkubo
National Institute for Materials Science (NIMS)
Research Center for Magnetic and Spintronic Materials
1-2-1 Sengen, Tsukuba, Ibaraki 305-0047, Japan
E-mail: ohkubo.Tadakatsu@nims.go.jp

Y. Kozuka
National Institute for Materials Science (NIMS)
Research Center for Materials Nanoarchitectonics (MANA)
1-1 Namiki, Tsukuba, Ibaraki 305-0044, Japan

K. Kimoto
National Institute for Materials Science (NIMS)
Center for Basic Research on Materials
1-2-1 Sengen, Tsukuba, Ibaraki 305-0047, Japan

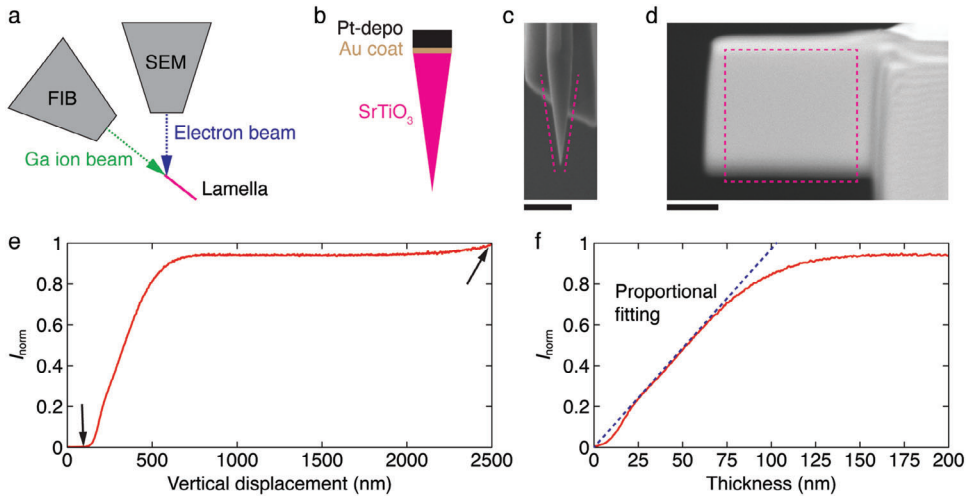

Figure 1. Thickness quantification of a $SrTiO_3$ crystal by BSE imaging. a) Schematic illustration of an FIB/SEM system. A lamella is tilted to the FIB's beam axis during a thinning process. b) Schematic illustration of a model chunk with a wedge shape. c) Side-view SEM image of a prepared chunk. The maximum thickness of the chunk is 560 nm. d) Front-view BSE image of the wedge-shaped chunk. The chunk is tilted to the FIB's beam axis. e) Profile of the normalized BSE intensity from the bottom edge to the top edge. The profile is cropped from the dotted region in (d) and averaged along the horizontal direction. f) The normalized BSE intensity is plotted as a function of thickness. Scale bars: 1 µm.

manual estimation of the lamella thickness is not quantitative but solely depends on the operator's expertise and skill.

Quantification of a lamella thickness from an SEM image has attracted considerable attention for the robust preparation of a thin STEM lamella. Ref. [23] reports that secondary-electron (SE) imaging can quantify the thickness of a Si lamella in a range above 20 nm. Refs. [24, 25] show the quantification of a lamella thickness above 50 nm by combining back-scattered-electron (BSE) imaging with Monte Carlo simulation. The other reports show the experimental quantification of a thick lamella (≈ 100 nm) by STEM in SEM[26] and four-dimensional STEM.[27] In general, SE imaging is sensitive to surface conditions, whereas BSE imaging reflects on the material's contrast due to the atomic number and density of the sample.[28] Repetitive SEM imaging in an FIB thinning process may cause surface contamination and surface charging, both of which affect the intensity of SE imaging. For this reason, BSE imaging may benefit the stability of thickness quantification in the lamella preparation process.

However, the quantification of a lamella thickness from the intensity is unmatured. The previous studies depend on the reference to Monte Carlo simulation in the thickness quantification, where the experimental validation covers only two thickness points of 50 and 100 nm.[24,25] It is not experimentally confirmed if the BSE imaging can quantify the lamella thickness below 20 nm. Recently, Skoupy et al. have experimentally studied the BSE intensity of a thin film grown on a substrate.[29] The normalized intensity of the BSE image linearly increases as the film thickness increases from 0 to 10 nm.[29] The linear response and its sensitivity near zero thickness suggest that BSE imaging may be able to quantify the thickness of a thin lamella. We point out that the pioneering study by Skoupy et al. acquires the BSE image of a flat sample without tilting. In contrast, a STEM lamella is usually tilted during an FIB thinning process (Figure 1a). The tilt effect on the BSE image of a lamella should be carefully considered since the BSE generation mechanism depends on the incident beam's angle and detection angle.[28,29] Thus, SEM experiments are needed to establish the thickness quantification of a tilted lamella from BSE imaging. Furthermore, the key challenge is addressed to realize the nanometer-level controllability of a lamella thickness for aberration-corrected STEM investigations. Real-time feedback from the thickness quantification to the FIB thinning process should be implemented and validated in a workflow of preparing a high-quality thin lamella.

Here, we demonstrate the robust preparation of sub-20-nm thin lamellae by FIB/SEM with real-time feedback from thickness quantification. First, we show that BSE imaging can quantify a lamella thickness from 0 to 100 nm without any references to numerical simulation. Then, we implement a real-time feedback program that terminates the FIB thinning if the lamella thickness reaches a target thickness. The real-time feedback leads to the nanometer-level controllability of the lamella thickness. Using this novel FIB/SEM methodology, a near-10-nm-thin lamella has been prepared from a $SrTiO_3$ single crystal. Aberration-corrected STEM confirms the thinness and quality of the prepared lamella. Moreover, we demonstrate that our methodology can prepare a thin lamella from a targeted heterointerface. Our methodology solves the fundamental difficulty in the robust preparation of a sub-20-nm-thin lamella from various materials.

2. Results and Discussion

2.1. Quantifying a Lamella Thickness by SEM

First, we study the quantitative relationship between the BSE intensity and the lamella thickness of a $SrTiO_3$ single crystal as a standard material. A wedge-shaped chunk is prepared from a $SrTiO_3$ single crystal by FIB (see Figures 1b,c and Experimental Section). Because this model chunk has flat surfaces, the distance

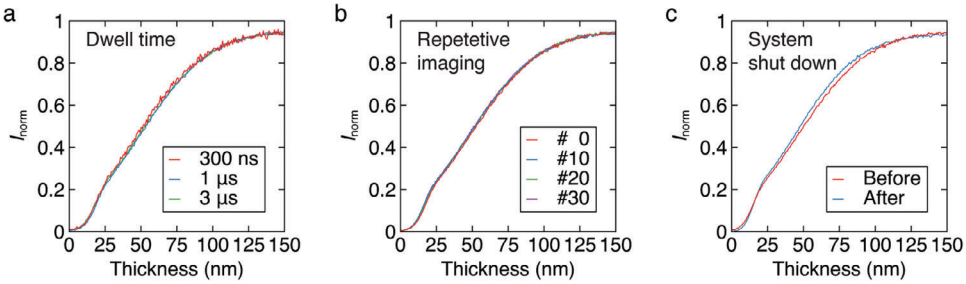

Figure 2. Stability of the thickness quantification of a $SrTiO_3$ chunk. The impact of the SEM settings on the thickness quantification of a $SrTiO_3$ chunk is investigated. a) Impact of dwell time. b) Impact of repetitive acquisitions of BSE images. A single BSE image of the 10th, 20th, and 30th acquisition is analyzed. c) Impact of system shutdown. The BSE image was acquired from the same chunk after the entire shutdown of the FIB/SEM system.

from the bottom edge is proportional to the local thickness. This model experiment allows a direct comparison between the BSE intensity and the local thickness.

Figure 1d shows the BSE image of the wedge-shaped chunk that is tilted to the FIB's beam axis. The BSE intensity is almost constant in the selected area, while the intensity gradually decreases from the bottom edge to the vacuum region. The monotonic change between the two intensity levels allows robust normalization of the BSE image as $I_{norm} = (I_{raw} - I_{min})/(I_{max} - I_{min})$, where I_{norm} and I_{raw} are the normalized and raw BSE intensity of the chunk and I_{min} and I_{max} are the minimum and maximum intensity in the selected region of Figure 1d. Hence, Figure 1e plots the normalized BSE intensity profile along the vertical displacement.

We aim to extract the relationship between the normalized BSE intensity and the thickness. So, the vertical displacement (y) is rescaled to the thickness (d) by the following protocol. i) Maximum displacement (y_{max}) is defined as the displacement at the interface between the $SrTiO_3$ substrate and the Pt-deposition layer. This displacement can be identified in the I_{norm} profile of Figure 1e (see the slight increase of I_{norm} at the right arrow). ii) Edge displacement (y_0) is defined as the displacement of the thin bottom edge (the left arrow in Figure 1e). For the accurate determination, we fit the BSE intensity profile as a linear function in the fitting range of $0.4 < I_{norm} < 0.6$. The edge displacement is identified as the displacement where the fitting function has $I_{norm} = 0$. iii) Maximum thickness (d_{max}) is defined as the chunk thickness at $y = y_{max}$. This thickness can be measured in the side-view SEM image (Figure 1c). iv) Finally, the vertical displacement is rescaled to the thickness as $d = d_{max} \times (y - y_0)/(y_{max} - y_0)$.

Figure 1f shows the normalized BSE intensity as a function of thickness. The normalized BSE intensity has a sensitivity to the thickness from 0 to ≈ 100 nm. More importantly, the normalized BSE intensity is proportional to the thickness in a range from 0 to 80 nm. Lamella preparation usually needs thickness quantification when the lamella thickness is below 100 nm. Thus, we simplify the thickness quantification model as $I_{norm} = \eta d$, where η is a coefficient to convert the normalized BSE intensity to the thickness. In our experiment of Figure 1f, we obtain $\eta = 0.0098$ (nm^{-1}) for a $SrTiO_3$ crystal by the proportional fitting in a range of $0.4 < I_{norm} < 0.6$. Note that the proportional fit has a slight difference from the I_{norm} plot in the range of $0 < I_{norm} < 0.2$. This is due to the roundness at the tip of the wedge-shaped chunk. In a later part of this study, the direct comparison with the EELS thickness confirms the accuracy of the thickness quantification from BSE imaging.

2.2. Robustness of Thickness Quantification

We investigate the robustness of the thickness quantification by BSE imaging. **Figure 2** analyzes the BSE images of the same $SrTiO_3$ chunk with different SEM parameters. The dwell time of image acquisition directly changes the raw BSE intensities and impacts surface charging. Nonetheless, the normalized BSE intensity is significantly robust to these settings (Figure 2a). Repetitive acquisitions of SEM images are essential during an FIB thinning process. Such repetitive acquisitions could lead to charging or surface contamination. Figure 2b compares the BSE images of the $SrTiO_3$ chunk over repetitive acquisitions of 30 images. The normalized BSE intensity receives a negligible impact from the repetitive BSE acquisitions. Thus, the temporal change of the normalized BSE intensity is directly linked with the thickness change of the lamella. To guarantee the quantitative repeatability of the BSE imaging, we reproduced the BSE imaging after the FIB/SEM system was completely shut down for maintenance (Figure 2c). These systematic experiments highlight the significant robustness of the thickness quantification by BSE imaging.

We also apply the thickness quantification method to various materials of single-crystalline substrates. Wedge-shaped chunks were prepared from Si, sapphire, and MgO substrates. BSE images were acquired from the chunks with a tilted geometry (Figure 1a). The normalized BSE intensity is plotted as a function of thickness for each of the materials (**Figure 3**). Proportional fitting is commonly valid in a thickness range from 0 to 100 nm, while the SEM acceleration voltage should be tuned for each material. This is because BSE imaging reflects on the material's contrast due to the atomic number and density of the sample.[28] As the SEM acceleration voltage increases, the incident electron beam penetrates into a lamella deeper, increasing the sensitivity to a thicker region.

Thus, we have established the robust quantification of lamella thickness by BSE imaging. The quantification methodology presents notable advantages over the existing methods. First, the measurable thickness ranges from 0 nm, which is necessary for the nanometer-level thickness controllability in the preparation of a sub-20-nm-thin lamella. Second, the quantification model has a simplicity of $I_{norm} = \eta d$, where the proportional coefficient η

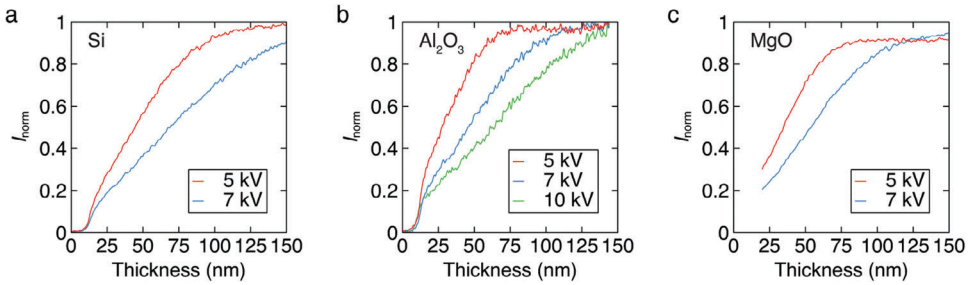

Figure 3. Thickness quantification of various materials by BSE imaging. Thickness quantification by BSE imaging is applied to various materials. The impact of the SEM acceleration voltage is also compared among 5 kV, 7 kV, and 10 kV. a) a Si single crystal. b) a sapphire crystal. c) a MgO single crystal. Since the tip of the MgO chunk is bending, the data near zero thickness is removed. The coefficients η of these plots are summarized in Table S1 (Supporting Information).

abstracts all knowledge about the relationship between the thickness and SEM intensity. Third, the coefficient η can be experimentally determined by imaging a wedge-shaped chunk without any reference to numerical simulation. Fourth, the thickness quantification is reproducible. Finally, the thickness quantification is applicable to a broad range of materials. So, our methodology solves the fundamental difficulty of thickness quantification in preparing a thin lamella.

2.3. Real-Time Feedback to FIB

Our method to quantify the lamella thickness is integrated with FIB thinning. We implement a real-time feedback program that autonomously terminates an FIB thinning process when the lamella thickness reaches a target thickness. **Figure 4** explains the feedback loop of our program. Initially, a user defines a thinning region in an FIB image, a targeted region, and a reference region in an SEM image, and the parameters of η, the thinning interval, and the target thickness (d_{stop}). A BSE image is acquired when the control program starts operation. The reference covers the thickest and the vacuum regions, which provide I_{max} and I_{min} for normalization, respectively. The BSE intensity averaged in the target region is normalized to I_{norm}. The local thickness (d) of the target region is calculated as $d = I_{norm}/\eta$. If $d \geqslant d_{stop}$, the control program executes the sequence of the FIB thinning with the pre-defined interval and the updating of the BSE image. If $d < d_{stop}$, the control program terminates the FIB thinning. In this way, our program determines the termination of the FIB thinning based on the real-time feedback of the quantified lamella thickness.

We experimentally confirm that the real-time feedback system controls the thickness of a $SrTiO_3$ lamella in an FIB thinning process (**Figure 5**). The FIB acceleration voltage of our experiments is 8 kV, considering a good balance between the sharp beam profile (Figure 4b) and the low damage to the lamella surface (Figure S1 in Supporting Information). The target thickness d_{stop} is fixed at 18 nm. Figure 5a,b shows a typical process of the 8 kV-FIB thinning. The thickness of an initial lamella monotonically decreases from $d = 63.3$ nm ($t = 0$ s) and stops at $d = 17.6$ nm ($t = 18$ s). Since the target thickness is 18 nm, the real-time feedback system terminates the FIB thinning as expected.

The statistical repeatability of the real-time feedback system is investigated. Figure 5c shows the thickness of eight lamellae

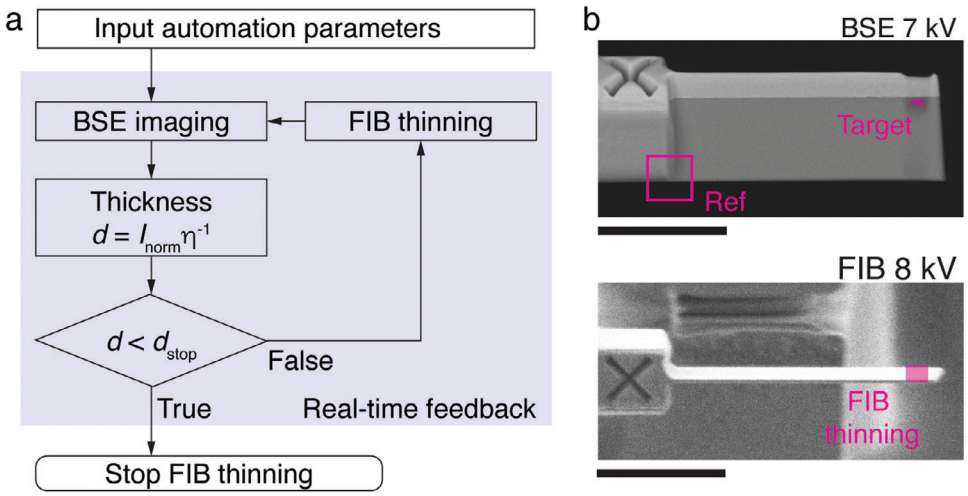

Figure 4. Real-time feedback of lamella thickness to the FIB termination. a) Feedback program to determine the termination of an FIB thinning process. b) Setup of automation parameters. The target region and reference region are defined in the BSE image. The thinning region is defined in the FIB image. Scale bar: 5 μm.

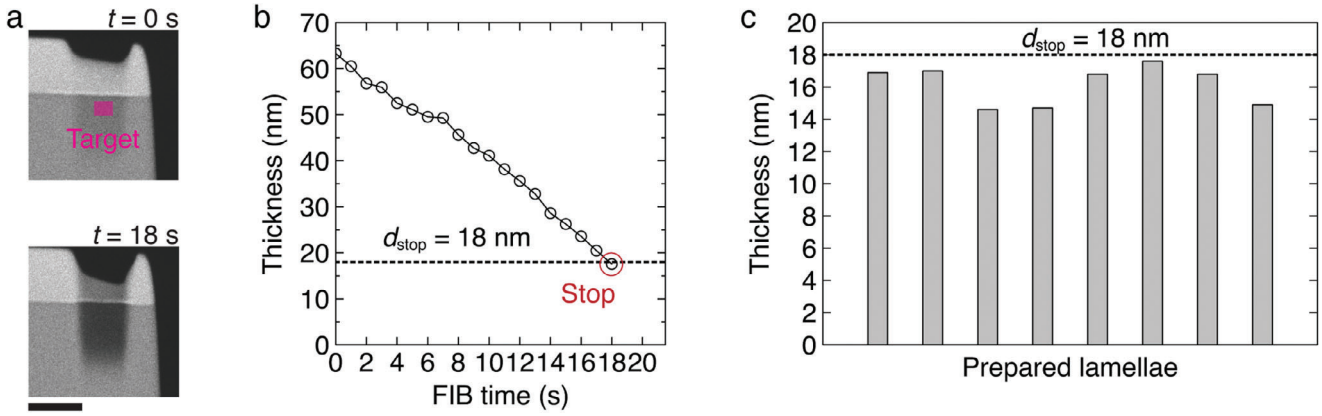

Figure 5. Controllability of a lamella thickness using the real-time feedback. a) A typical process of the 8 kV-FIB thinning with real-time feedback to the FIB termination. BSE images were acquired every 1 second of the FIB thinning time. b) The temporal change of the lamella thickness during the 8 kV-FIB thinning. Our real-time feedback system terminated the FIB thinning when the thickness reached 17.6 nm at t = 18 s. c) Repeatability of the lamella thickness at which our feedback system terminated the FIB thinning. Scale bar: 1 µm.

after the 8 kV-FIB thinning with the real-time feedback of the thickness quantification. The average thickness among the eight lamellae is 16.2 nm ±1.2 nm, almost equal to d_{stop} = 18 nm. In Figure 5b, the thinning rate is calculated as 2.5 nm s^{-1}. The thickness deviation of 1.2 nm is half of the thickness that the FIB thins in a pre-defined interval (1 s). Thus, one can improve the thickness controllability by slowing down the thinning rate (e.g., lowering the FIB current). Taken together, the real-time feedback of the thickness quantification provides one-nanometer-level controllability of the lamella thickness during an FIB thinning process.

2.4. Workflow of Lamella Preparation

The FIB thinning with the real-time feedback is applied to the workflow of lamella preparation. A common workflow to prepare a high-quality lamella has three major steps in its thinning process: i) preparing an initial lamella with a thickness of ≈ 100 nm (**Figure 6a**), ii) low-damage thinning of the lamella (Figure 6b), and iii) the final cleaning of the surface damage (Figure 6c). Among these three steps, the controllability of the lamella thickness has a critical impact on the low-damage thinning process. Thus, the real-time feedback system is used in the low-damage thinning process of our workflow (Figure 6b).

Our workflow is designed as follows. An initial lamella is prepared using the automated protocol presented in Ref. [22]. Commercial software automatically operates the rough-milling process, the lift-out process, and the 30 kV-FIB thinning process. The nominal thickness of the 30 kV-FIB thinning is set at 120 nm (Figure 6a). Note that the nominal thickness is the spatial gap between two FIB-milling boxes, not the measured thickness of an actual lamella.[22] Next, the 8 kV-FIB thins both sides of the initial lamella down to a sub-20-nm thickness by using the real-time

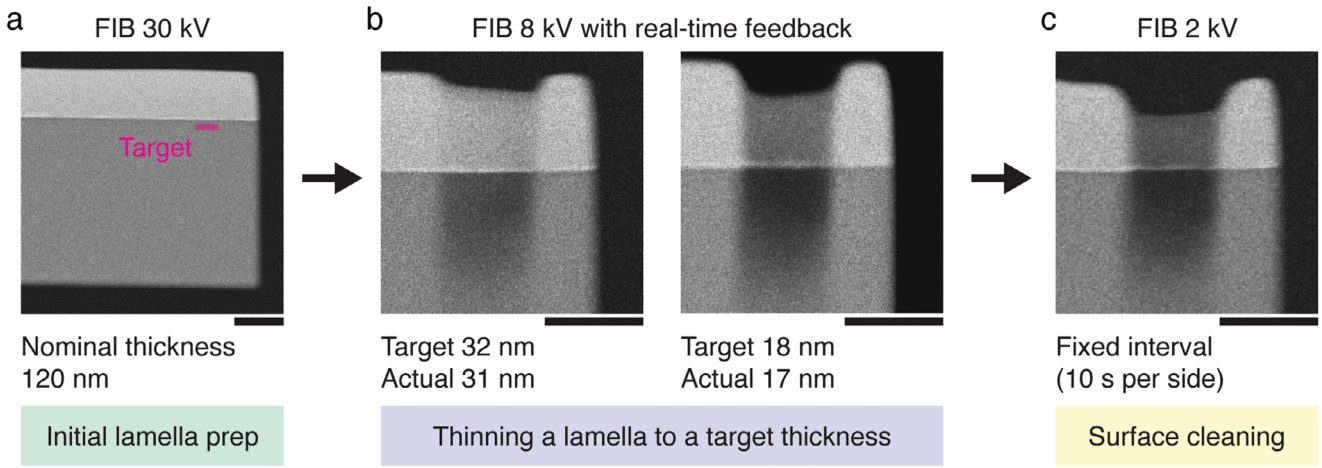

Figure 6. Workflow of preparing a thin lamella from a $SrTiO_3$ single crystal. a) Preparation of an initial lamella. b) The 8 kV-FIB thinning of both sides of the lamella using our real-time feedback program. The FIB mode and its current are cleaning cross section (CCS) and 26 pA, respectively. The over-tilt angles of the 8 kV-FIB processes are −3.0° (the first process) and +2.5° (the second process). c) Manual cleaning by the 2 kV-FIB with rectangle FIB mode and a beam current of 17 pA. The over-tilt angles are +7.0° (the first process) and −7.0° (the second process). The termination criterion of the 2 kV-FIB is a fixed interval of 10 s per side. Scale bars: 1µm.

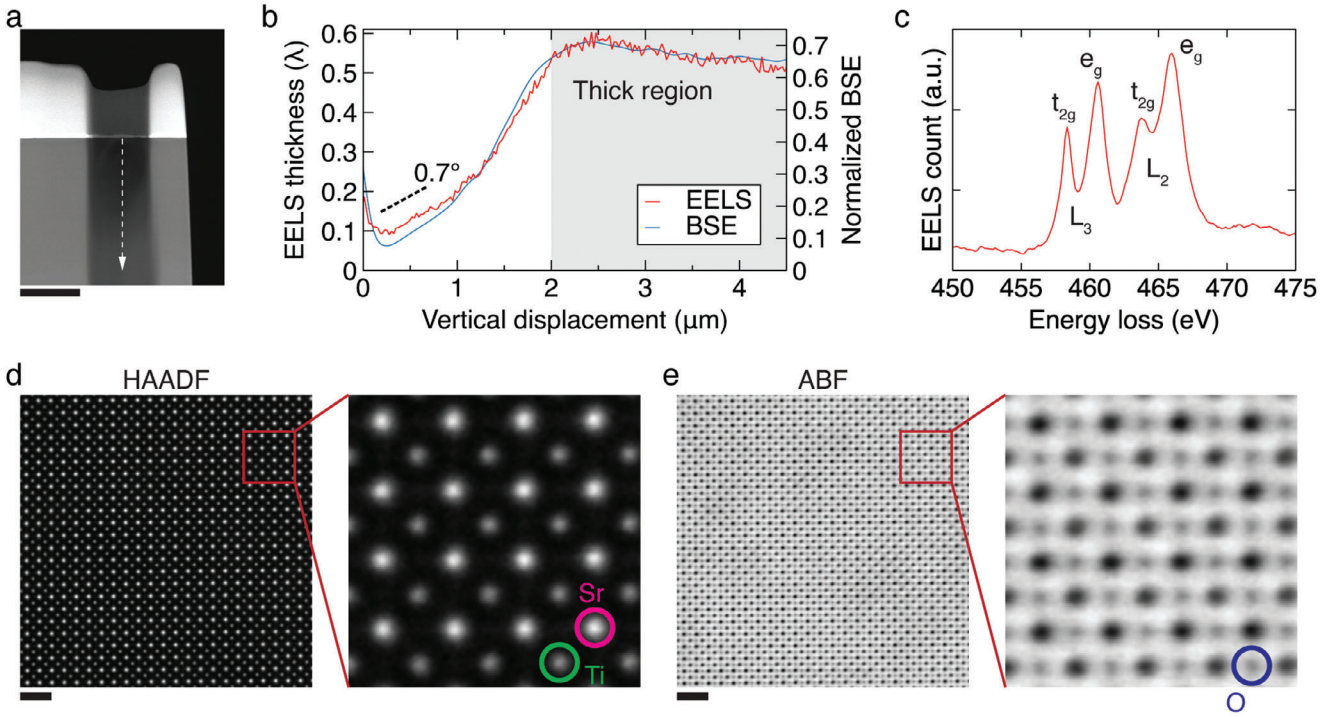

Figure 7. STEM evaluation of the lamella prepared from a $SrTiO_3$ single crystal. a) HAADF-STEM image of the prepared lamella. b) EELS thickness profile along the vertical axis in panel (a). Vertical displacement is 0 nm at the interface between the top protective layer and the $SrTiO_3$ crystal. The profile of normalized BSE intensity (I_{norm}) is quantified from the BSE image in Figure 6c. The dotted line indicates the thickness gradient with a taper angle of 0.7°. c) Monochromated EELS of Ti-L edge was acquired in the thinnest region. d) and e) Atomic-level HAADF and ABF images were simultaneously acquired in the thinnest region. All images are unfiltered. Scale bars: 1μm (a) and 1 nm (d and e).

feedback system (Figure 6b). The first 8 kV-FIB process thins one side of the lamella, where the target thickness is 32 nm. The second 8 kV-FIB process thins the other side of the lamella, where the target thickness is 18 nm. Because our real-time feedback system provides the one-nanometer-level controllability of the lamella thickness, the lamella has the actual thickness of 31 and 17 nm after the first and second thinning processes, respectively (Figure 6b). Finally, the 2 kV-FIB cleans both sides of the lamella to minimize the surface damage. The operation of the 2 kV-FIB cleaning is manual and terminated by a pre-defined interval (10 s per side). Figure 6c shows the BSE image acquired after the 2 kV-FIB cleaning. The lamella has a thickness of 8 nm in the thinnest region (**Figure** 7b). Thus, we have successfully prepared a near-10-nm-thin lamella from a $SrTiO_3$ crystal by the workflow mentioned above.

We also check if our workflow can minimize the surface damage of the lamella. Figure S1 (Supporting Information) shows that the depth of the FIB's damage is ≈ 10 nm and below 2 nm when the FIB acceleration voltage is 30 and 8 kV, respectively. Thus, the thickness targets in the initial lamella preparation (120 nm) and the low-damage thinning (18 nm) are reasonable from the viewpoint of damage management. In the final cleaning process, the 2 kV-FIB decreases the surface damage within an atomic layer per side (Figure S1c in Supporting Information). The lamella thickness of 8 nm equals 21 atomic layers of $SrTiO_3$ crystal. Thus, the prepared lamella may have a notable balance between the thinness and minimum surface damage.

2.5. STEM Evaluation of the $SrTiO_3$ Lamella

Aberration-corrected STEM imaging and monochromated EELS evaluate the thinness and crystalline quality of the $SrTiO_3$ lamella prepared by our workflow. The thickness profile across the lamella is extracted from the EELS zero-loss peak (Figure 7a and b). The EELS thickness of the lamella ranges from 0.09λ = 9 nm to 0.60λ = 58 nm, where λ is the mean free path of a 300 keV electron and has its value of 97 nm in $SrTiO_3$. We compare the EELS thickness with the thickness quantified from the BSE image in the same lamella. The EELS thickness profile overlaps with the normalized BSE intensity of the lamella (Figure 7b). This result supports the thickness quantification model of $I_{norm} = \eta d$ (see Figure 1). The thinnest region in the lamella has $I_{norm} = 0.077$, which can be converted to the thickness as $d = I_{norm}/\eta = 8$ nm. The thickness quantified from BSE imaging mostly matches the EELS thickness in the thinnest region. Considering the simplicity of our quantification model, the accuracy of quantifying the lamella thickness from the BSE image is notable.

Next, we evaluate the crystalline quality of the prepared lamella in its thinnest region. Figure 7c shows that both peaks of Ti-L_2 and Ti-L_3 split in the EEL spectrum. These splits are the signature of the symmetric TiO_2 octahedra in a $SrTiO_3$ crystal.[30] Figure 7d, 7e, and Figure S5 (Supporting Information) show the atomic-level STEM images acquired in the thinnest region of the lamella. In the high-angle annular dark-field (HAADF) image, titanium

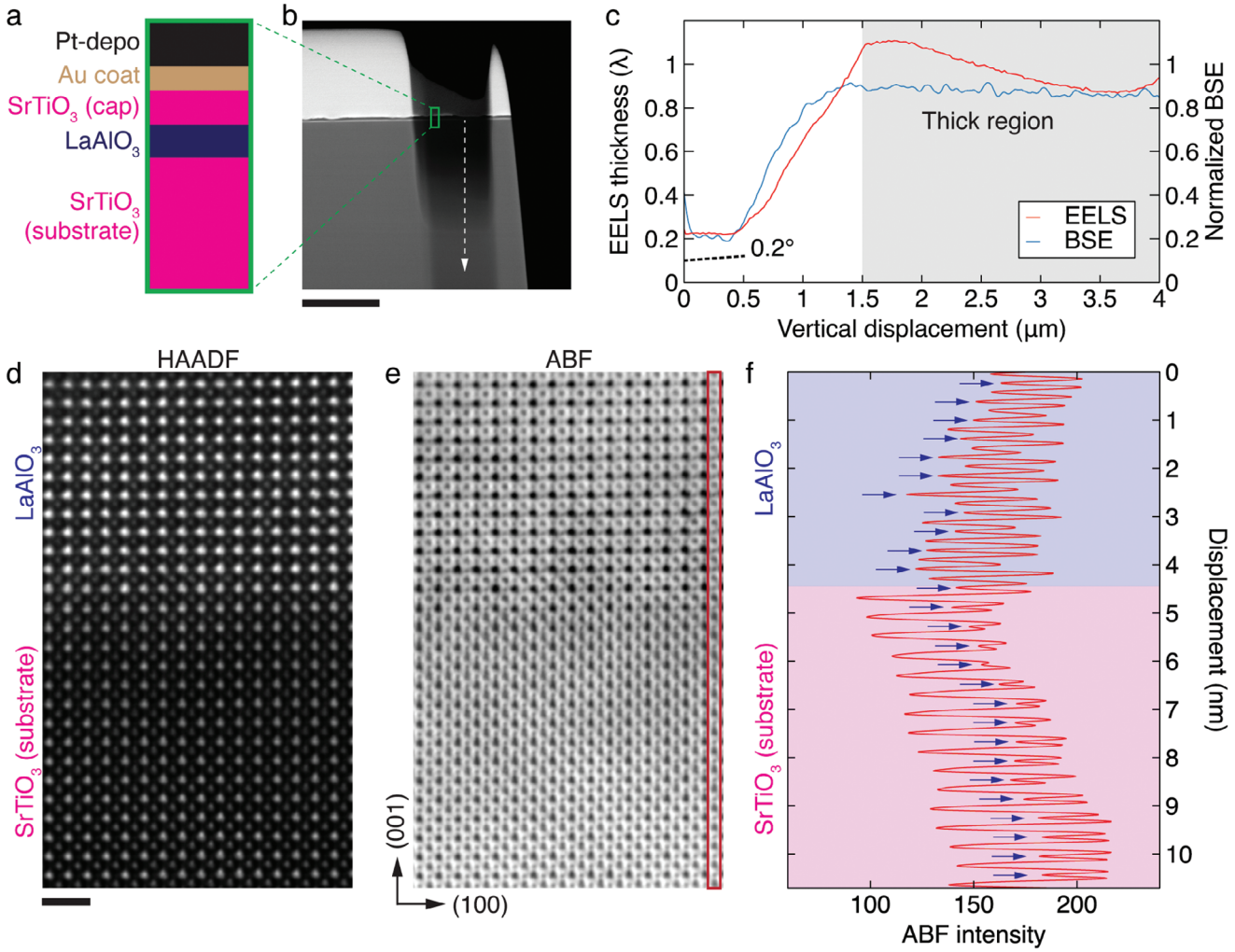

Figure 8. STEM evaluation of a thin lamella prepared from $LaAlO_3/SrTiO_3$ heterostructure interface. a) Schematic of the $LaAlO_3/SrTiO_3$ heterostructure grown on a $SrTiO_3$ substrate. The $LaAlO_3$ layer has a thickness of 20 nm and is capped with another $SrTiO_3$ layer. b) HAADF-STEM image of the lamella. The green box indicates the position of the heterostructure interface. c) EELS thickness profile from the heterointerface along the vertical direction (see the arrow in (b)). The thickness profile of the same lamella is also quantified from the BSE image acquired after all preparation processes (see Figure S3 in Supporting Information). The dotted line indicates the thickness gradient with a taper angle of 0.2°. d) and e) Atomic-level HAADF and ABF images were acquired at the interface between the $LaAlO_3$ layer and the $SrTiO_3$ substrate. Both images are unfiltered. Figure S2b (Supporting Information) shows an atomic-level iDPC image of the heterostructure interface. f) The intensity profile of the ABF image (see the red mark in (e)). The arrows indicate the positions of oxygen atoms. Scale bars: 1 μm (b) and 1 nm (d).

and strontium atoms are visualized, whereas oxygen atoms are hardly visible (Figure 7d). Due to its sensitivity to the light elements, the annular bright-field (ABF) image complementarily visualizes the oxygen atoms in the $SrTiO_3$ lamella (Figure 7e). An integrated differential phase contrast (iDPC) image of the lamella also visualizes the oxygen atoms (Figure S2a in Supporting Information).

These STEM results confirm that the thinness and crystal quality of the lamella are suitable for aberration-corrected STEM investigations. In other words, our workflow has a suitable design for i) the control of the lamella thickness and ii) the damage management in the lamella preparation.

2.6. Targeting a Heterointerface

We apply our methodology to a heterointerface to cover many STEM studies. As designed in Figure 4, our real-time feedback program monitors the lamella thickness "at any region" that a user selects. Thus, the lamella thickness at a heterointerface may be controllable by selecting the target region near the target heterointerface. As a model case, our methodology is applied to an epitaxial heterostructure of $LaAlO_3$ grown on a $SrTiO_3$ (001) substrate (see Experimental section and **Figure 8a**). Epitaxial heterostructures and superlattices on $SrTiO_3$ have been intensively studied as a platform for creating emergent phenomena in complex oxides.[31–40]

In our experiment, a sub-20-nm-thin lamella is prepared from the $LaAlO_3/SrTiO_3$ heterointerface by our workflow in Figure 6. The 8 kV-FIB thinning process is controlled by the real-time feedback system. The target region is set at the $SrTiO_3$ substrate region slightly below the heterointerface (Figure S3a in Supporting Information). We aim to control the lamella thickness at the $LaAlO_3/SrTiO_3$ heterointerface by controlling the lamella thickness in the substrate region. As shown in Figure S3 (Supporting Information), our workflow has successfully prepared a thin lamella from the heterostructural sample. Note that the target thickness of the 8 kV-thinning is changed to 29 nm because the FIB's damage to a $LaAlO_3$ crystal is not precisely known.

Aberration-corrected STEM evaluates the lamella prepared from the heterointerface. Figure 8c shows the EELS thickness profile from the heterointerface to the $SrTiO_3$ substrate. The thickness profile is mostly flat near the target heterointerface. Thus, our methodology can control the lamella thickness of a heterointerface by controlling the lamella thickness at the substrate. The EELS thickness near the heterointerface is $0.2\lambda = 19$ nm. The normalized BSE intensity in the thinnest region is $I_{norm} = 0.19$, which is converted to the thickness of $I_{norm}/\eta = 19$ nm (Figure 8c). In addition, the EELS thickness profile of the lamella mostly fits the profile of the thickness quantified by BSE imaging. This confirms, again, that the thickness quantification from BSE imaging is accurate.

Atomic-level STEM images of the heterointerface are shown in Figure 8d. The HAADF image visualizes the atoms of strontium, titanium, lanthanum, and aluminum in the heterointerface. The ABF and iDPC images also visualize the oxygen atoms in the heterointerface (Figures 8e and f and Figure S2b in Supporting Information). The position of each atomic column at the heterointerface addresses the distortion and rotation of the local crystalline lattice, which links with emergent phenomena in complex oxides.[31–40] In addition to the atomic-level imaging, we show the layer-resolved EELS mapping in the heterointerface (Figure S4 in Supporting Information). The EELS elemental mapping shows that the $LaAlO_3/SrTiO_3$ heterostructure has a sharp interface. We also analyze the spectral change of the Ti-L edge across the heterointerface. The peaks of Ti-L_2 and Ti-L_3 edge split in both the $SrTiO_3$ substrate and the $SrTiO_3$ cap layer. Thus, the prepared lamella retains the highly crystalline structure of $SrTiO_3$ at the heterointerface.

These STEM results confirm that the prepared lamella has suitable thinness and high crystalline quality "at the target heterointerface." In addition, we have already shown that our methodology can quantify the lamella thickness of standard substrates (Figure 3). Therefore, our methodology is applicable to various heterointerfaces grown on a standard substrate.

2.7. Broad Impact to STEM Studies

Aberration-corrected STEM has been advancing its resolution,[2,5] sensitivity to light elements,[6–8] and EELS microanalysis[9–16] due to the intensive demand for atomic-level microstructural investigations. The state-of-the-art STEM methodologies require the preparation of a thin lamella. For example, the state-of-the-art imaging of electron ptychography records the highest resolution of 23 pm.[5] Electron ptychography severely requires that the lamella thickness is 20 nm or below because multiple scattering of the electron beam inside a lamella leads to the loss of spatial resolution.[5,41,42] When this highest-resolution imaging is applied to a heterointerface, the lamella thickness "at the interface" should be strictly controlled in a sub-20-nm range. Such preparation is very difficult by the existing FIB/SEM methodology because an operator estimates the lamella thickness without quantitative image analysis. In contrast, our methodology quantifies the lamella thickness near the target heterointerface. Real-time feedback of the local thickness realizes one-nanometer-level controllability of the lamella thickness at the heterointerface. Moreover, our methodology does not need special expertise for the preparation of a sub-20-nm-thin lamella at a specific heterointerface. Hence, the preparation methodology in our study will broaden the applications of state-of-the-art STEM methodologies.

While this study focuses on the thickness range below 20 nm, some of the STEM studies accept a relatively thick lamella. HAADF imaging and energy-dispersive X-ray analysis are less sensitive to lamella thickness than state-of-the-art STEM techniques. In our experiments, the BSE imaging can quantify the lamella thickness up to 80 nm (upper thickness of the proportional fitting in Figure 1f). Thus, our real-time feedback system offers on-demand control of the lamella thickness only if the target thickness fits the measurable range. A notable advantage of our methodology is that a user can determine the lamella thickness as a given parameter. All expertise about the thickness quantification is summarized into one coefficient of η. Unlike previous studies,[24,25] the parameter η can be experimentally determined from a wedge-shaped chunk (Figure 1). In addition, the thickness quantified from BSE imaging is robust and compatible with the EELS thickness. Thus, a user can predict if the lamella has a suitable thickness "before" the STEM investigation. These advances should help many STEM studies, especially in the case that an operator is a non-expert.

Moreover, our novel FIB/SEM methodology should impact the FIB/SEM automation in materials science,[22] biological science,[43] and the semiconductor industry.[44] The existing technologies of FIB/SEM automation cover the rough-milling, liftout, and thinning processes but do not quantify lamella thickness from SEM imaging in the final thinning process. Thus, the existing automation of FIB/SEM causes the discrepancy between the nominal thickness and the actual thickness.[22,43] The discrepancy is typically in the order of 10 nm. As demonstrated in Figure 5, our real-time feedback system provides one-nanometer-level controllability of lamella thickness. Combining this methodology with the existing automation technology will significantly enhance the controllability of the lamella thickness, driving the shift from a manual FIB/SEM to an automatic FIB/SEM.

3. Conclusion

This study solves fundamental difficulties in preparing a high-quality sub-20-nm-thin lamella for aberration-corrected STEM. We establish a robust methodology to quantify a lamella thickness by BSE imaging (Figures 1-3). The thickness quantification provides feedback to determine the termination of

an FIB thinning process in lamella preparation (Figure 4), leading to one-nanometer-level controllability of lamella thickness (Figure 5). Using the real-time feedback system, we have successfully prepared a near-10-nm-thin lamella from a $SrTiO_3$ crystal (Figures 6 and 7). We also demonstrate that our methodology is applicable to a STEM study of a heterointerface grown on a standard substrate (Figure 8). Therefore, the methodology presented in our study offers a robust and operator-independent platform to prepare a thin lamella from various materials. This platform will broadly impact aberration-corrected STEM studies in materials science[1,2] and the semiconductor industry.[3,4]

4. Experimental Section

FIB/SEM System: An FIB/SEM DualBeam system (Helios 5 UX, Thermo Fisher Scientific) was used. The real-time feedback system with Python script was implemented. The script was run through AutoScript 4 (Thermo Fisher Scientific). Note a recent demonstration of script-based FIB/SEM automation to prepare a sharp needle for atom probe tomography.[45] The study autonomously determines the termination of FIB milling of a needle by the feedback of SEM imaging, using the FIB/SEM platform of Helios 5 UX and Python scripting.

SEM Imaging: To quantify the thickness of a lamella or a wedge-shaped chunk, BSE images were acquired by a high-resolution SEM integrated with Helios 5 UX. Immersion-lens mode was chosen and an in-lens detector of Through-Lens-Detector (TLD) with BSE mode was used. Acceleration voltage, beam current, and dwell time were set at 7 kV, 0.8 nA, and 1 µs, respectively. When acquiring an SEM image, a lamella (or a wedge-shaped chunk) was tilted to the FIB's beam axis. The SEM's defocus is negligible to the BSE intensity profile along the tilted direction. See also Figure S6 in Supporting Information.

Preparing a Wedge-Shaped Chunk: Wedge-shaped chunks were prepared from $SrTiO_3$, Si, sapphire, and MgO by the following procedure. First, gold was sputtered to a substrate to avoid charging up. Second, a protective layer was made on the substrate by FIB deposition. Third, FIB cut a micron-sized chunk in the substrate and transferred the chunk to a TEM grid by an in-situ manipulator. Finally, the FIB at 30 kV milled the chunk with an over-tilt angle of $\pm 7.0°$. The flatness of the chunk surfaces was carefully checked by a side-view SEM and a thickness quantification from a 10 kV-BSE image.

Preparing a Thin Lamella: Initially, gold was sputtered to a $SrTiO_3$ substrate to avoid charging up. Pt-deposition, rough-milling, lift-out, and the 30 kV-FIB thinning processes were operated by following the methods of Ref. [22]. The 8 kV-FIB thinning process was controlled by the real-time feedback system that we implemented. To quantify lamella thickness from BSE imaging, the conversion coefficient η is set at 0.0098 nm^{-1} (see Figure 1). Note that the over-tilt angle was tuned to minimize the thickness gradient in the lamella from the top protective layer to the bottom edge. The 2 kV-FIB finally cleaned the surfaces of a lamella.

STEM Analysis: Titan Cubed (Thermo Fisher Scientific) with aberration correctors and a monochromator was used. The acceleration voltage was set at 300 kV. EELS data were acquired by a spectrometer (Continuum, Gatan) with Titan Cubed. iDPC images were acquired by a 4-segmented STEM detector and analysis software (Velox, Thermo Fisher Scientific). We also used Titan200 ChemiSTEM (Thermo Fisher Scientific) for the aberration-corrected STEM analysis operated at 200 kV. EELS thickness is calculated from the zero-loss peak intensity of the measured spectra using Digital Micrograph software (Gatan).[11] The mean free path of a 300 keV electron was set at 97 nm in the thickness analysis of the $SrTiO_3$ lamella.

Synthesis of $LaAlO_3/SrTiO_3$ Heterostructure: $LaAlO_3$ was synthesized on a single crystal of $SrTiO_3$ by pulsed laser deposition at 550°C under an oxygen partial pressure of 1 mTorr with a laser frequency and energy of 5 Hz and 13 mJ per pulse using a fourth harmonic wave of a Nd:YAG laser. The thickness of the $LaAlO_3$ was 20 nm. The $LaAlO_3$ was capped by $SrTiO_3$.

Supporting Information

Supporting Information is available from the Wiley Online Library or from the author.

Acknowledgements

The authors thank Kyoko Suzuki and Atsuya Kurita for experimental support and Smart Solutions Corporation for supporting the implementation of codes. Y.K. was financially supported by JST FOREST Program (Grant Number: JPMJFR203D), and MANA, World Premier International Research Center Initiative (WPI), MEXT, Japan. K.K. was financially supported by a Grant-in-Aid for Transformative Research Areas (A) 'Supraceramics' (JSPS KAKENHI Grant Numbers JP 22H05145). This work was supported by MEXT Program: Data Creation and Utilization-Type Material Research and Development Project (Digital Transformation Initiative Center for Magnetic Materials) Grant Number JPMXP1122715503.

Conflict of Interest

The authors declare no conflict of interest.

Author Contributions

H.T., J.U., and T.O. conceptualized the study and developed the FIB/SEM software. H.T. and J.U. prepared lamellae. Y.K. synthesized materials. J.U. and K.K. performed STEM measurements. H.T. curated the data and wrote the manuscript. All authors discussed the results and commented on the manuscript.

Data Availability Statement

The data that support the findings of this study are available from the corresponding author upon reasonable request.

Keywords

aberration-corrected STEM, FIB/SEM, lamella preparation, SEM imaging, thickness quantification

Received: October 17, 2023
Revised: January 24, 2024
Published online:

[1] S. J. Pennycook, P. D. Nellist, *Scanning Transmission Electron Microscopy: Imaging and Analysis*, Springer Science & Business Media, Spring St, NY **2011**.
[2] S. J. Pennycook, C. Li, M. Li, C. Tang, E. Okunishi, M. Varela, Y.-M. Kim, J. H. Jang, *J. Anal. Sci. Technol.* **2018**, *9*, 1.
[3] N. G. Orji, M. Badaroglu, B. M. Barnes, C. Beitia, B. D. Bunday, U. Celano, R. J. Kline, M. Neisser, Y. Obeng, A. Vladar, *Nat. Electron.* **2018**, *1*, 532.
[4] Z. Zhang, W. Wang, Z. Dong, X. Yang, F. Liang, X. Chen, C. Wang, C. Luo, J. Zhang, X. Wu, L. Sun, J. Chu, *Adv. Electron. Mater.* **2022**, *8*, 2101401.
[5] Z. Chen, Y. Jiang, Y.-T. Shao, M. E. Holtz, M. Odstrčil, M. Guizar-Sicairos, I. Hanke, S. Ganschow, D. G. Schlom, D. A. Muller, *Science* **2021**, *372*, 826.

[6] R. Ishikawa, E. Okunishi, H. Sawada, Y. Kondo, F. Hosokawa, E. Abe, *Nat. Mater.* **2011**, *10*, 278.
[7] N. Shibata, S. D. Findlay, Y. Kohno, H. Sawada, Y. Kondo, Y. Ikuhara, *Nat. Phys.* **2012**, *8*, 611.
[8] S. de Graaf, J. Momand, C. Mitterbauer, S. Lazar, B. J. Kooi, *Sci. Adv.* **2020**, *6*, eaay4312.
[9] K. Kimoto, T. Asaka, T. Nagai, M. Saito, Y. Matsui, K. Ishizuka, *Nature* **2007**, *450*, 702.
[10] D. Muller, L. F. Kourkoutis, M. Murfitt, J. Song, H. Hwang, J. Silcox, N. Dellby, O. Krivanek, *Science* **2008**, *319*, 1073.
[11] R. F. Egerton, *Electron Energy-loss Spectroscopy in the Electron Microscope*, Springer Science & Business Media, NY **2011**.
[12] O. L. Krivanek, T. C. Lovejoy, N. Dellby, T. Aoki, R. Carpenter, P. Rez, E. Soignard, J. Zhu, P. E. Batson, M. J. Lagos, R. F. Egerton, P. Crozier, *Nature* **2014**, *514*, 209.
[13] R. Qi, R. Shi, Y. Li, Y. Sun, M. Wu, N. Li, J. Du, K. Liu, C. Chen, J. Chen, F. Wang, D. Yu, E.-G. Wang, P. Gao, *Nature* **2021**, *599*, 399.
[14] J. Kikkawa, T. Taniguchi, K. Kimoto, *Phys. Rev. B* **2021**, *104*, L201402.
[15] Y.-H. Li, R.-S. Qi, R.-C. Shi, J.-N. Hu, Z.-T. Liu, Y.-W. Sun, M.-Q. Li, N. Li, C.-L. Song, L. Wang, Z.-B. Hao, Y. Luo, Q.-K. Xue, X.-C. Ma, P. Gao, *Proc. Natl. Acad. Sci.* **2022**, *119*, e2117027119.
[16] C. A. Gadre, X. Yan, Q. Song, J. Li, L. Gu, H. Huyan, T. Aoki, S.-W. Lee, G. Chen, R. Wu, X. Pan, *Nature* **2022**, *606*, 292.
[17] L. A. Giannuzzi, F. A. Stevie, *Introduction to Focused Ion Beams: Instrumentation, Theory, Techniques and Practice*, Springer Science & Business Media, NY **2005**.
[18] C. A. Volkert, A. M. Minor, *MRS Bull.* **2007**, *32*, 389.
[19] J. Mayer, L. A. Giannuzzi, T. Kamino, J. Michael, *MRS Bull.* **2007**, *32*, 400.
[20] M. Schaffer, B. Schaffer, Q. Ramasse, *Ultramicroscopy* **2012**, *114*, 62.
[21] H. Wang, V. Srot, B. Fenk, G. Laskin, J. Mannhart, P. A. van Aken, *Micron* **2021**, *140*, 102979.
[22] H. Tsurusawa, N. Nakanishi, K. Kawano, Y. Chen, M. Dutka, B. Van Leer, T. Mizoguchi, *Sci. Rep.* **2021**, *11*, 1.
[23] A. Conlan, E. Tillotson, A. Rakowski, D. Cooper, S. Haigh, *J. Microscopy* **2020**, *279*, 168.
[24] R. Salzer, A. Graff, M. Simon, F. Altmann, *Microsc. Microanal.* **2009**, *15*, 340.
[25] T. Volkenandt, F. Pérez-Willard, M. Rauscher, P. M. Anger, *Microsc. Microanal.* **2017**, *23*, 304.
[26] R. Young, A. Buxbaum, B. Peterson, R. Schampers, in *Proceedings of the 34th International Symposium for Testing and Failure Analysis*, **2008**, pp. 320–326.
[27] R. Skoupỳ, D. B. Boltje, M. Slouf, K. Mrázová, T. Láznička, C. M. Taisne, V. Krzyžánek, J. P. Hoogenboom, A. J. Jakobi, *Small Methods* **2023**, 2300258.
[28] J. I. Goldstein, D. E. Newbury, J. R. Michael, N. W. Ritchie, J. H. J. Scott, D. C. Joy, *Scanning Electron Microscopy and X-ray Microanalysis*, Springer Science & Business Media, NY **2017**.
[29] R. Skoupy, T. Fort, V. Krzyzanek, *Nanomaterials* **2020**, *10*, 332.
[30] E. Stoyanov, F. Langenhorst, G. Steinle-Neumann, *Am. Mineral.* **2007**, *92*, 577.
[31] A. Ohtomo, H. Hwang, *Nature* **2004**, *427*, 423.
[32] D. A. Muller, N. Nakagawa, A. Ohtomo, J. L. Grazul, H. Y. Hwang, *Nature* **2004**, *430*, 657.
[33] H. Y. Hwang, Y. Iwasa, M. Kawasaki, B. Keimer, N. Nagaosa, Y. Tokura, *Nat. Mater.* **2012**, *11*, 103.
[34] C. Cantoni, J. Gazquez, F. Miletto Granozio, M. P. Oxley, M. Varela, A. R. Lupini, S. J. Pennycook, C. Aruta, U. S. di Uccio, P. Perna, D. Maccariello, *Adv. Mater.* **2012**, *24*, 3952.
[35] Q. He, R. Ishikawa, A. R. Lupini, L. Qiao, E. J. Moon, O. Ovchinnikov, S. J. May, M. D. Biegalski, A. Y. Borisevich, *ACS Nano* **2015**, *9*, 8412.
[36] K. Song, S. Ryu, H. Lee, T. R. Paudel, C. T. Koch, B. Park, J. K. Lee, S.-Y. Choi, Y.-M. Kim, J. C. Kim, H. Y. Jeong, M. S. Rzchowski, E. Y. Tsymbal, C.-B. Eom, S. H. Oh, *Nat. Nanotechnol.* **2018**, *13*, 198.
[37] R. Ramesh, D. G. Schlom, *Nat. Rev. Mater.* **2019**, *4*, 257.
[38] D.-S. Park, A. Rata, I. Maznichenko, S. Ostanin, Y. Gan, S. Agrestini, G. Rees, M. Walker, J. Li, J. Herrero-Martin, G. Singh, Z. Luo, A. Bhatnagar, Y. Z. Chen, V. Tileli, P. Muralt, A. Kalaboukhov, I. Mertig, K. Dörr, A. Ernst, N. Pryds, *Nat. Commun.* **2020**, *11*, 3650.
[39] K. Song, T. Min, J. Seo, S. Ryu, H. Lee, Z. Wang, S.-Y. Choi, J. Lee, C.-B. Eom, S. H. Oh, *Adv. Sci.* **2021**, *8*, 2002073.
[40] T. Min, W. Choi, J. Seo, G. Han, K. Song, S. Ryu, H. Lee, J. Lee, K. Eom, C.-B. Eom, H. Y. Jeong, Y.-M. Kim, J. Lee, S. H. Oh, *Sci. Adv.* **2021**, *7*, eabe9053.
[41] H. Sha, J. Cui, R. Yu, *Sci. Adv.* **2022**, *8*, eabn2275.
[42] H. Sha, Y. Ma, G. Cao, J. Cui, W. Yang, Q. Li, R. Yu, *Nat. Commun.* **2023**, *14*, 162.
[43] C. Berger, M. Dumoux, T. Glen, N. B.-y. Yee, J. M. Mitchels, Z. Patáková, M. C. Darrow, J. H. Naismith, M. Grange, *Nat. Commun.* **2023**, *14*, 629.
[44] A. Kenslea, C. Hakala, Z. Zhong, Y. Lu, J. Fretwell, J. Hager, C. Kang, H. Tan, W. Weng, L. Dumas, I. Brooks, in *2018 29th Annual SEMI Advanced Semiconductor Manufacturing Conference (ASMC)*, IEEE, New York **2018**, pp. 324–327.
[45] J. Uzuhashi, T. Ohkubo, K. Hono, *Ultramicroscopy* **2023**, *247*, 113704.

